A&A 392, 395–406 (2002)
DOI: 10.1051/0004-6361:20020861

Astronomy & Astrophysics

The K20 survey

III. Photometric and spectroscopic properties of the sample⋆

A. Cimatti[1], M. Mignoli[2], E. Daddi[3], L. Pozzetti[2], A. Fontana[4], P. Saracco[5], F. Poli[6], A. Renzini[3], G. Zamorani[2], T. Broadhurst[7], S. Cristiani[8,9], S. D'Odorico[3], E. Giallongo[4], R. Gilmozzi[3], and N. Menci[4]

[1] Istituto Nazionale di Astrofisica, Osservatorio Astrofisico di Arcetri, Largo E. Fermi 5, 50125 Firenze, Italy
[2] Istituto Nazionale di Astrofisica, Osservatorio Astronomico di Bologna, via Ranzani 1, 40127 Bologna, Italy
[3] European Southern Observatory, Karl-Schwarzschild-Str. 2, 85748 Garching, Germany
[4] Istituto Nazionale di Astrofisica, Osservatorio Astronomico di Roma, via Dell'Osservatorio 2, Monteporzio, Italy
[5] Istituto Nazionale di Astrofisica, Osservatorio Astronomico di Brera, via E. Bianchi 46, Merate, Italy
[6] Dipartimento di Astronomia, Università "La Sapienza", Roma, Italy
[7] Racah Institute for Physics, The Hebrew University, Jerusalem 91904, Israel
[8] ST, European Coordinating Facility, Karl-Schwarzschild-Str. 2, 85748 Garching, Germany
[9] Istituto Nazionale di Astrofisica, Osservatorio Astronomico di Trieste, Via Tiepolo 11, 34131 Trieste, Italy

Received 5 April 2002 / Accepted 6 June 2002

Abstract. The K20 survey is an ESO VLT optical and near-infrared spectroscopic survey aimed at obtaining spectral information and redshifts of a complete sample of about 550 objects to $K_s \leq 20.0$ over two independent fields with a total area of 52 arcmin^2. In this paper we discuss the scientific motivation of such a survey, we describe the photometric and spectroscopic properties of the sample, and we release the K_s-band photometric catalog. Extensive simulations showed that the sample is photometrically highly complete to $K_s = 20$. The observed galaxy counts and the $R - K_s$ color distribution are consistent with literature results. We observed spectroscopically 94% of the sample, reaching a spectroscopic redshift identification completeness of 92% to $K_s \leq 20.0$ for the observed targets, and of 87% for the whole sample (i.e. counting also the unobserved targets). Deep spectroscopy was complemented with multi-band deep imaging in order to derive tested and reliable photometric redshifts for the galaxies lacking spectroscopic redshifts. The results show a very good agreement between the spectroscopic and the photometric redshifts with $< z_{spe} - z_{phot} > = 0.01$ and with a dispersion of $\sigma_{\Delta z} = 0.09$. Using both the spectroscopic and the photometric redshifts, we reached an overall redshift completeness of about 98%. The size of the sample, the redshift completeness, the availability of high quality photometric redshifts and multicolor spectral energy distributions make the K20 survey database one of the most complete samples available to date for constraining the currently competing scenarios of galaxy formation and for a variety of other galaxy evolution studies.

Key words. galaxies: evolution; galaxies: formation

1. Introduction

Contrary to surveys for high-z galaxies selected in the optical, which are more sensitive to the star-formation activity, the selection of galaxies in the K-band has the important advantage of not being affected by strong K-correction effects. This is due to the similarity of the different galaxy spectral types in the near-infrared. Cowie et al. (1994) showed that over a broad range of redshifts the K-correction amplitude in the K-band is much smaller than those in I- or in B- bands, and very little dependent on the galaxy spectral types (from elliptical to irregular galaxies). Thus, the great advantage of a K-band selection is that the resulting samples are almost free from strong selection effects and do not critically depend on the galaxy types as in optical samples.

However, deriving the complete redshift distribution of a sample of faint K-band selected galaxies is a challenging goal even for 8–10 m class telescopes. Indeed, a fraction of the galaxies are beyond the spectroscopic limits (e.g. very red galaxies with $R > 26$) and/or lie in a redshift range where the spectra do not present prominent features in the observer frame (e.g. the redshift "desert" at $1.4 < z < 2.0$ for optical spectroscopy).

Songaila et al. (1994) carried out an optical spectroscopic survey of K-selected galaxies at different magnitude depths over a wide range of field sizes (from ∼0.4 deg^2 down to

Send offprint requests to: A. Cimatti,
e-mail: cimatti@arcetri.astro.it

⋆ Based on observations made at the European Southern Observatory, Paranal, Chile (ESO LP 164.O-0560).

$K \lesssim 15$, to ∼5 arcmin^2 to $K \lesssim 20$) reaching an identification completeness of ∼70% at $K \sim 19-20$. Cowie et al. (1996) performed with the Keck I 10 m telescope a deeper optical spectroscopic survey of galaxies with $K < 20$ over a field of 26.2 arcmin^2, reaching a spectroscopic identification completeness of ∼60% at $K \sim 20$. Cohen et al. (1999a, 1999b) observed a sample of 195 objects over an area of 14.6 arcmin^2 reaching a spectroscopic completeness of 83.6% to $K_s < 20$. A large spectroscopic survey is currently in progress over four independent fields covering a total area of about 100 arcmin^2 to $K < 20$ (Stern et al. 2001).

In addition to purely spectroscopic surveys, a number of more recent projects made use mostly of photometric redshifts. For instance, Drory et al. (2001) selected ∼5000 galaxies to $K < 19$ over 998 arcmin^2, and estimated the photometric redshifts for 94% of them using *VRIJK* photometry (spectroscopic redshifts were available for only ∼6% of the sample). Other surveys based largely on photometric redshifts range from that of Firth et al. (2002), who covered a field of 744 arcmin^2 to $H < 20.0-20.5$ and derived photometric redshifts for about 4000 galaxies using *UBVRIH* photometry, to those of e.g. Fontana et al. (1999, 2000) and Rudnick et al. (2001) based on very deep observations (typically to $K_s < 21-23$) of very small fields (a few arcmin^2).

Surveys for faint galaxies selected in the *K*-band are very important to investigate the formation and evolution of galaxies.

One of the main questions of galaxy evolution is whether massive galaxies (e.g. $\mathcal{M}_{\rm stars} \gtrsim 10^{11}\ M_\odot$) are the late product of merging of pre-existing disk galaxies occurring mostly at $z < 1.5-2$, as predicted by the current CDM scenarios (e.g. Kauffmann et al. 1993, 1996; Cole et al. 2000; Baugh et al. 1996; Somerville et al. 2001, Baugh et al. 2002, and references therein), or whether they formed at $z > 2-3$ during a short-lived and single event of vigorous star formation, followed by a passive evolution (or pure luminosity evolution, PLE) of the stellar population to nowadays (see e.g. Renzini 1999; Renzini & Cimatti 1999; Peebles 2002, for recent reviews).

Since the near-IR light is a good tracer of a galaxy stellar mass (Gavazzi et al. 1996; Madau et al. 1998; Kauffmann & Charlot 1998, KC98 hereafter), the above scenarios can in principle be tested by selecting galaxies at 2.2 μm in the *K*-band and deriving their redshift distribution and physical and evolutionary properties (e.g. Broadhurst et al. 1992).

KC98 estimated that ∼60% and ∼10% of the galaxies in a $K < 20$ sample are expected to be at $z > 1$, respectively, in a PLE and in a standard CDM hierarchical merging model (cf. their Fig. 4). Such a large difference was in fact one of the main motivations of our original project to undertake a complete redshift survey for all objects with $K < 20$ in a small area of the sky. However, more recent models consistently show that for $z > 1$ the difference between the predictions of different scenarios is less extreme than in the KC98 realization (Menci et al., Pozzetti et al., in preparation; see also Firth et al. 2002). Part of the effect is due to the now favored ΛCDM cosmology which pushes most of the merging activity in hierarchical models at earlier times compared to τCDM and SCDM models, and therefore get closer to the PLE case. Moreover, a different tuning of the star-formation algorithms (to accomodate for more star formation at high-*z*) also reduces the differences between the two scenarios (e.g. Somerville et al. 2001).

In order to address the question of the formation and evolution of galaxies and to constrain the current models, we performed a new spectroscopic survey of *K*-selected galaxies with the ESO VLT. In this paper, we present the main scientific motivations, we define the sample selection, we discuss the photometry, the completeness, we present the main spectroscopic and photometric redshift results, and we release the K_s-band photometric catalog. The spectral and multicolor catalogs will be presented elsewhere together with the forthcoming papers on the scientific analysis of the sample. Magnitudes are given in Vega system. The widely accepted cosmology with $H_0 = 70$ km s^{-1} Mpc^{-1}, $\Omega_m = 0.3$ and $\Omega_\Lambda = 0.7$ is adopted throughout this paper.

2. The K20 survey

In order to overcome the limitations of the previous surveys (e.g. small samples and/or spectroscopic incompleteness), we started in 1999 a project that was dubbed "K20 survey". To such project, 17 nights were allocated as an ESO VLT Large Program distributed over a period of two years (see also `http://www.arcetri.astro.it/~k20/` for more details).

The survey aims at obtaining spectroscopic redshifts with the highest possible completeness for a sizeable sample of field galaxies with $K_s < 20$. The main scientific aim of the K20 survey is to probe the evolution of galaxies to $z \gtrsim 1$, deriving their redshift distribution, luminosity function and stellar mass function. This body of observational evidences is being and will be used for a comparison with the different models of galaxy formation and evolution.

To this purpose, deep optical and near-infrared spectroscopy were complemented by deep multi-band imaging in order to derive tested and reliable photometric redshifts for the unavoidable fraction of galaxies with no spectroscopic redshifts.

Besides such a main goal, the K20 survey was also designed to address other important issues such as: (1) the nature of Extremely Red Objects (EROs), (2) the evolution of elliptical galaxies, (3) the evolution of galaxy clustering, (4) the spectral properties of a large number of galaxies and their evolution as a function of redshift, (5) the evolution of the volume star formation density, (6) the fraction of AGN in *K*-selected samples, (7) the optimization of the photometric redshift techniques based on ground-based imaging, and (8) the brown dwarf population at high Galactic latitude. The K20 database will also provide important information to complement other multiwavelength surveys performed in the same fields, such as the SIRTF GOODS (`http://www.stsci.edu/science/goods`) and SWIRE (`http://www.ipac.caltech.edu/SWIRE/`) projects.

Two papers based on the K20 survey have been already published showing an application of our database to investigate the nature and the clustering of the EROs (Cimatti et al. 2002; Daddi et al. 2002).

Table 1. The K_s-band images of the target fields.

Field	Center Coordinates (J2000)	Field Size (arcmin^2)	Seeing (*FWHM*)	Int. time (hours)	Gal. Coord.	A_V (mag)	A_K (mag)
QSO 0055-269	$00^h57^m58.91^s$ $-26°43'12.1''$	19.8	$0.9''$	3.93	$197.7°$ $-88.5°$	0.065	0.007
CDFS	$03^h32^m22.52^s$ $-27°46'23.5''$	32.2	$0.8''$	3.0	$223.5°$ $-54.5°$	0.028	0.003

The sample was selected from two independent fields in order to reduce the effects of the field-to-field variations. The targets were extracted from a sub-area of the Chandra Deep Field South (CDFS; Giacconi et al. 2001) and from a field centered around the QSO 0055-269 at $z = 3.656$ (see Table 1 for details). The total sample includes 546 objects over 52 arcmin^2 selected on the basis of the single criterion of $K_s \leq 20.0$. Adopting the K-correction effects derived from the Bruzual & Charlot (1993) spectral synthesis models (GISSEL version 2000, hereafter BC2000), an apparent magnitude of $K_s = 20.0$ corresponds to rest-frame typical absolute magnitudes of $M_{K_s} \sim -21.7$ and $M_{K_s} \sim -23.4$ for $z = 0.5$ and $z = 1.0$ respectively, with a weak dependence on the galaxy type because of the small K-correction effects. Such absolute magnitudes correspond to $\sim 0.1 L_K^*$ and $\sim 0.4 L_K^*$ respectively (adopting the L_K^* of the Cole et al. 2001 near-IR local luminosity function of galaxies). Since the stellar mass-to-infrared luminosity ratio ($\mathcal{M}_{\rm stars}/L_K$) is relatively insensitive to the star formation history, the limiting K_s-band luminosities of our survey can be converted into the corresponding limiting stellar masses. As the stellar population ages, $\mathcal{M}_{\rm stars}/L_K$ (in solar units) remains very close to unity, independent of the galaxy color and Hubble type, and has a weak dependence on z.

According to the mean stellar mass-to-light ratio and representative stellar mass $\mathcal{M}^*_{\rm stars}$ in the local universe (Cole et al. 2001), and adopting the predictions of the BC2000 spectral synthesis models, the limiting stellar masses corresponding to $K_s = 20$, for the Salpeter IMF, are about $\mathcal{M}_{\rm stars} > 10^{10} M_\odot \simeq 0.07 \mathcal{M}^*_{\rm stars}$ and $\mathcal{M}_{\rm stars} > 4 \times 10^{10} M_\odot \simeq 0.3 \mathcal{M}^*_{\rm stars}$ for $z = 0.5$ and $z = 1$ respectively.

3. Near-infrared imaging

For both fields, the K_s-band images were obtained with the ESO NTT equipped with SOFI (Moorwood et al. 1998) with a pixel size of $0.29''$ and under photometric conditions (see also Rengelink et al. 1998 for more details on observations and database for the CDFS).

Since the ESO Imaging Survey (EIS; `http://www.eso.org/science/eis/`) public JK_s images of the CDFS available at the time of the K20 sample selection were affected by a loss of the flux up to 0.3 magnitudes at the faint limit of our survey, we performed a new independent reduction and calibration of the CDFS K_s-band image.

The K_s-band data of the CDFS and the JK_s data of the 0055-2659 field were reduced in a standard manner using the IRAF[1] software package DIMSUM[2]. Raw frames were first corrected for bias and dark current by subtracting a median dark frame, and flat-fielded using an average differential sky light flat-field image. After deriving a master mask frame with DIMSUM, a sky background image for each frame was obtained by averaging a set (from 6 to 10) of time adjacent frames where the sources were masked out. The sky-subtracted frames were then inspected in order to reject or to correct the frames with bad sky residuals, and the flux of bright objects visible in the individual frames was monitored to verify the photometric conditions and to reject discrepant frames if necessary. The final sky-subtracted frames were rescaled to the same airmass and photometric zero-point, shifted and coadded together to generate the final image. The photometric calibration was achieved through the observation of standard stars from the Persson et al. (1998) sample. The Galactic extinction was estimated using the maps of Schlegel et al. (1998) (see Table 1).

4. Photometry and completeness of the sample

4.1. Source extraction and photometry

The sample was extracted from the K_s-band images using the SExtractor package (Bertin & Arnouts 1996). After convolving the images with a Gaussian function matching the measured seeing *FWHM*, the objects exceeding a $S/N > 2.2$ over the background noise in a minimum area of 10 pixels (i.e. 0.7σ/pixel) were extracted.

The total flux of the selected objects was then measured using the SExtractor BEST magnitude. Such a magnitude is defined to be either a Kron magnitude (Kron 1980), which is measured in an elliptical aperture whose size is determined by the profile of the object, or an isophotal magnitude for objects blended or in crowded fields (see Bertin & Arnouts 1996 for more details).

In both fields, the images are considerably deeper than the $K_s = 20$ threshold of the spectroscopic sample, thus minimizing both selections effects and biases in the estimated magnitudes. Typically, galaxies at the faint limit of our sample have $S/N \simeq 10$–15, according to the SExtractor noise estimate. The cases of blended objects were analysed in more detail in order to correct the total magnitudes for the effects of blending.

[1] IRAF is distributed by the National Optical Astronomy Observatories, which are operated by the Association of Universities for Research in Astronomy, Inc., under cooperative agreement with the National Science Foundation.

[2] Deep Infrared Mosaicing Software, a package written by Eisenhardt, Dickinson, Stanford and Ward, available at `ftp://iraf.noao.edu/contrib/dimsumV2`.

4.2. Photometric completeness

Since the goal of photometric surveys for faint galaxies is to measure their total integrated flux, the completeness is usually defined only by the total apparent magnitude. However, in practice it is well known that a fraction of the flux is lost when measuring magnitudes with aperture or isophotal photometry because of the finite size of the photometric apertures and a minimum area for object detection (e.g. Impey & Bothun 1997; Dalcanton 1998). The fraction of the lost light at the survey limiting flux depends on the size and on the surface brightness profile of the galaxies. Moreover, since the surface brightness of galaxies rapidly becomes fainter with increasing redshift as $(1+z)^{-4}$, this cosmological dimming could make many high-z galaxies undetectable below the adopted surface brightness threshold.

Thus, it is important to evaluate such potential selection effects in order to make a meaningful comparison between the observed properties of the sample and the model predictions of galaxy formation and evolution. We have therefore explored in our survey the effects due to the detection limits, i.e. surface brightness limit ($\mu_K \sim 23$ mag/arcsec^2) and minimum area (10 pixels), and to the procedure adopted for the photometric measurements, using both real and artificial galaxies.

4.2.1. Limiting surface brightness

Following Lilly et al. (1995), we show in Fig. 1 the surface brightness at the minimum detection radius, as a function of magnitude for all the objects in our survey. The vertical line marks the magnitude limit, $K_s < 20$, while the horizontal lines show the surface brightness limits used in the objects detection for the two fields (i.e. a source is detected only if its detection surface brightness is above the surface brightness limit). Most of the objects have surface brightness well above the nominal limit.

Figure 1 also shows the tracks expected for L^* and $10L^*$ elliptical and spiral galaxies. These tracks have been obtained using the observed relations between luminosity, effective radius and surface brightness for local spirals (Impey et al. 1996) and elliptical (Bender et al. 1992; Pahre 1999) galaxies, and taking into account the the effect of the seeing on the intrinsic galaxy profile (see Angeretti et al. 2002 for details). The adopted galaxy profile parameters are indicated in the figure caption. Note that at the faint limit of the sample, the L^* tracks are essentially parallel to the star locus because for these galaxies the observed profiles are dominated by the seeing. Figure 1 shows that the surface brightness selection effects are negligible for $L < 10L^*$ galaxies.

4.2.2. Adding artificial galaxies

In order to better assess the effects for different galaxy types, we applied a method consisting in the addition of artificial galaxies to the real images of our survey fields.

About 100 artificial galaxies were generated using the `artdata.mkobjects` software in IRAF. We used three morphological types (one de Vaucouleurs profile with axial ratio $b/a = 0.7$, and two exponential profiles with $b/a = 0.4$ and $b/a = 0.8$ respectively), and four intrinsic half-light radii for each morphology type ($r_e = 0.3''$, $0.6''$, $1.0''$, $1.5''$). The choice of such values for r_e was motivated by the quantitative morphological studies of faint galaxies which showed that objects with $r_e \gtrsim 1.0''$ are extremely rare (e.g. Marleau & Simard 1998).

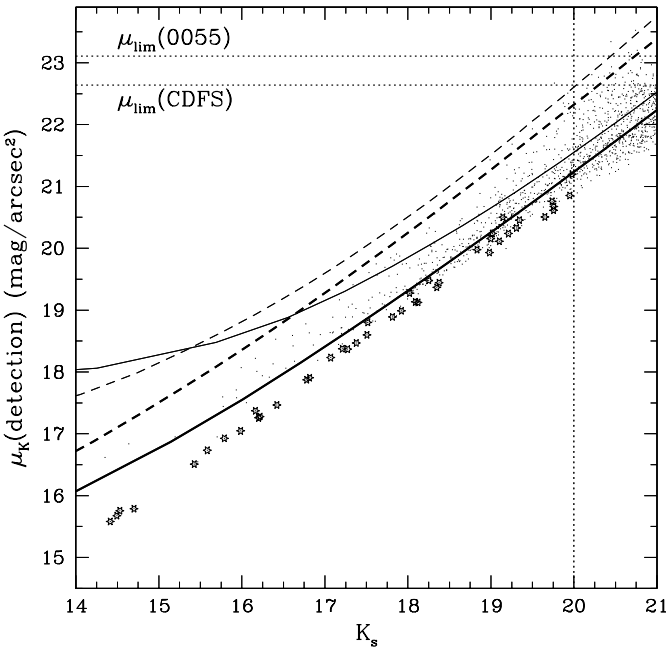

Fig. 1. Surface brightness at the minimum detection radius as a function of magnitude for all objects in the sample. The vertical dotted line represents the sample magnitude limit, $K_s < 20$, while the horizontal dotted lines indicate the limiting detection surface brightness in the two fields ($\mu_K \sim 22.64, 23.11$ mag/arcsec^2 in the CDFS and 0055-269 field respectively). The tracks indicate the expected behavior of elliptical (thick lines) and spiral (thin lines) galaxies for two representative luminosities (Kochanek et al. 2001): L^* (solid lines: $M_K^* = -24.3 + 5\log h_{70}$, $r_e = 3.1\ h_{70}^{-1}$ kpc for ellipticals and $M_K^* = -23.8 + 5\log h_{70}$, $r_e = 6.1\ h_{70}^{-1}$ kpc for spirals) and $10\ L^*$ (dashed lines: $M_K^* = -26.8 + 5\log h_{70}$, $r_e = 16.3\ h_{70}^{-1}$ for ellipticals and $M_K^* = -26.3 + 5\log h_{70}$, $r_e = 13.0\ h_{70}^{-1}$ for spirals). Star symbols represent the stars identified in our survey on the basis of their spectra.

Such 12 artificial galaxy models were then convolved with a PSF with a Moffat profile (as derived from field stars) and created for different magnitudes ($K_s = 18.0, 18.5, 19.0, 19.5, 20.0, 20.5$). In both fields, the results indicate that at $K_s = 20.0$ the completeness ($N_{recovered}/N_{input}$) is 100% for $r_e \leq 1.0''$, whereas it decreases to ~90% for $r_e = 1.5''$. We also verified that the results do not significantly change for other values of b/a.

Figures 2 and 3 show examples of the results of such simulation. The recovered magnitudes at $K_s \leq 20.0$ are generally consistent with the input ones for the exponential profile galaxies, but they turned out to be systematically underestimated for galaxies with a de Vaucouleurs profile (typically 0.1–0.3 magnitudes for $0.3'' \leq r_e \leq 1.0''$).

Such an effect was already discussed for example by Fasano et al. (1998), Dalcanton (1998) and Martini (2001). The origin of such an effect is due to the magnitudes being limited to an aperture which exclude the outermost regions of the

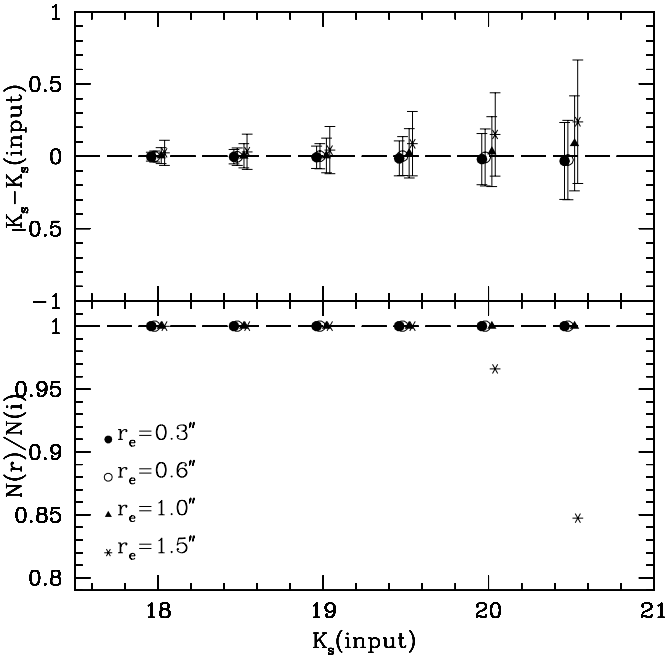

Fig. 2. The results of a simulation in the 0055-269 field made with artificial galaxies with de Vaucouleurs profiles, $b/a = 0.7$, four values of r_e and for 6 input magnitudes (K_s = 18.0, 18.5, 19.0, 19.5, 20.0, 20.5) (see text for more details). The top and the bottom panels show respectively the average difference between the measured (K_s) and the input magnitudes, and the fraction of the number of recovered objects, $N(r)$, to the number of input artificial objects, $N(i)$. The points are shifted along the abscissa around each of the 6 magnitudes to improve their visibility. Similar results are obtained for the CDFS.

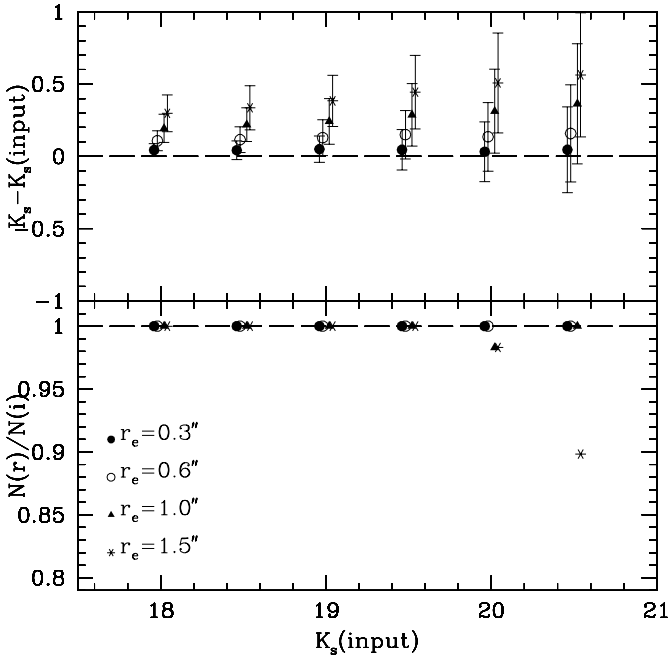

Fig. 3. Same as Fig. 2, but for a simulation in the 0055-269 field made with exponential profiles and $b/a = 0.4$ Similar results are obtained for the CDFS.

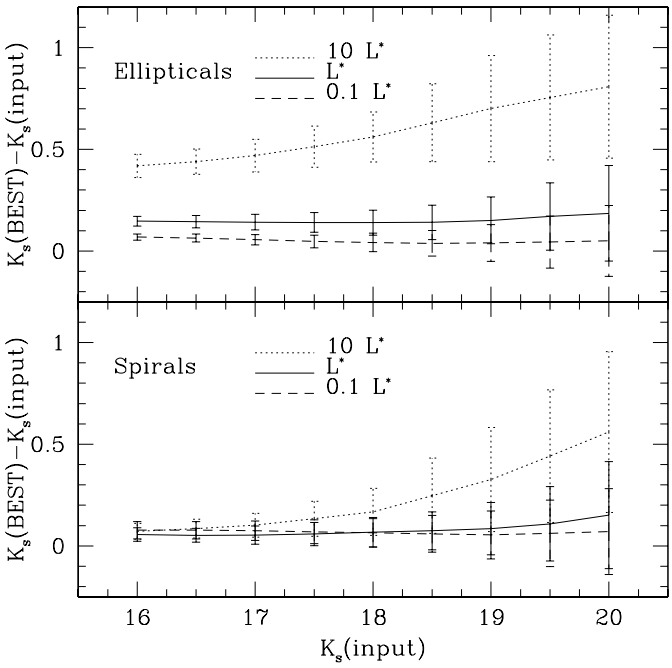

Fig. 4. A comparison of BEST magnitude from SExtractor and input magnitudes in our simulations for ellipticals (top panel) and spirals (bottom panel) in the CDFS. Different lines represent different luminosities, as indicated in the labels, and the error bars represent the dispersion in the simulations, using about 100 artificial galaxies at each magnitudes.

galaxy surface brightness profiles, and it does not depend on the software used for the automatic photometry.

While this is less critical for rapidly declining exponential profiles, its influence is larger for the more slowly decreasing de Vaucouleurs profiles. Being typically $r_e \lesssim 0.6''$ in high-z early-type galaxies (e.g. Fasano et al. 1998), this means that the underestimate in our sample is at most $\lesssim$0.2 magnitudes at $K_s = 20$ for galaxies with a de Vaucouleurs profile. The lack of HST imaging for the K20 sample prevented us from applying magnitude corrections for the galaxies with de Vaucouleurs profiles.

Figure 4 shows the same results as a function of the luminosity (adopting the luminosity-surface brigthness relations discussed in Sect. 4.2.1). For typical L^* ellipticals we could miss systematically up to 20% of the flux, and only <10–15% for exponential disks. Such effects become more relevant only for very large and high luminosity galaxies (e.g. $L \sim 10L^*$), but fortunately such objects are rare enough not to introduce severe selection effects in our survey.

Such selection effects will be taken into account in the next papers including the comparison with the predictions of galaxy formation models.

4.2.3. Dimming real galaxies

As an additional test on the completeness, we applied the method described by Saracco et al. (1999, 2001), consisting in dimming observed bright galaxies by various factors, while keeping the background noise constant and equal to that of the original image. In particular, all the objects were extracted from the original frame, kept with the same original sizes, scaled to a lower flux and then re-inserted in the real images. A new

Table 2. The differential galaxy counts.

K_s	$n_{0055-269}$	n_{CDFS}	n_{tot}	N_{tot}
13.75	$0^{+1.84}_{-0.00}$	$1^{+2.30}_{-0.83}$	$1^{+2.30}_{-0.83}$	$69.2^{+159.2}_{-57.5}$
14.25	$0^{+1.84}_{-0.00}$	$1^{+2.30}_{-0.83}$	$1^{+2.30}_{-0.83}$	$69.2^{+159.2}_{-57.5}$
14.75	$1^{+2.30}_{-0.83}$	$0^{+1.84}_{-0.00}$	$1^{+2.30}_{-0.83}$	$69.2^{+159.2}_{-57.5}$
15.25	$0^{+1.84}_{-0.00}$	$1^{+2.30}_{-0.83}$	$1^{+2.30}_{-0.83}$	$69.2^{+159.2}_{-57.5}$
15.75	$2^{+2.64}_{-1.29}$	$3^{+2.92}_{-2.37}$	$5^{+3.38}_{-2.16}$	$346.1^{+234.0}_{-149.5}$
16.25	$1^{+2.30}_{-0.83}$	$5^{+3.38}_{-2.16}$	$6^{+3.58}_{-2.38}$	$415.4^{+247.8}_{-164.8}$
16.75	$3^{+2.92}_{-2.37}$	$5^{+3.38}_{-2.16}$	$8^{+3.95}_{-2.77}$	$553.8^{+273.5}_{-191.8}$
17.25	$7^{+3.77}_{-2.58}$	$17^{+5.20}_{-4.08}$	$24^{+5.97}_{-4.86}$	$1661.5^{+413.3}_{-336.5}$
17.75	$15^{+4.96}_{-3.83}$	$22^{+5.76}_{-4.65}$	$37^{+7.14}_{-6.06}$	$2561.5^{+494.3}_{-419.5}$
18.25	$28^{+6.35}_{-5.26}$	$35^{+6.97}_{-5.89}$	$63^{+8.00}_{-7.91}$	$4361.5^{+553.8}_{-547.6}$
18.75	$29^{+6.45}_{-5.35}$	$59^{+7.75}_{-7.66}$	$88^{+9.43}_{-9.36}$	$6092.3^{+652.8}_{-648.0}$
19.25	$56^{+7.54}_{-7.46}$	$69^{+8.36}_{-8.28}$	$125^{+11.18}_{-11.18}$	$8653.8^{+774.0}_{-774.0}$
19.75	$43^{+7.61}_{-6.53}$	$86^{+9.33}_{-9.25}$	$129^{+11.36}_{-11.36}$	$8930.7^{+786.5}_{-786.5}$

K_s: bin central magnitude;
n_{0055}: number of galaxies in the 0055-269 field with 1σ Poissonian uncertainties;
n_{CDFS}: number of galaxies in the CDFS with 1σ Poissonian uncertainties;
n_{tot}: total number of galaxies with 1σ Poissonian uncertainties;
N_{tot}: gal/deg^2/0.5 mag (both fields) with 1σ Poissonian uncertainties.

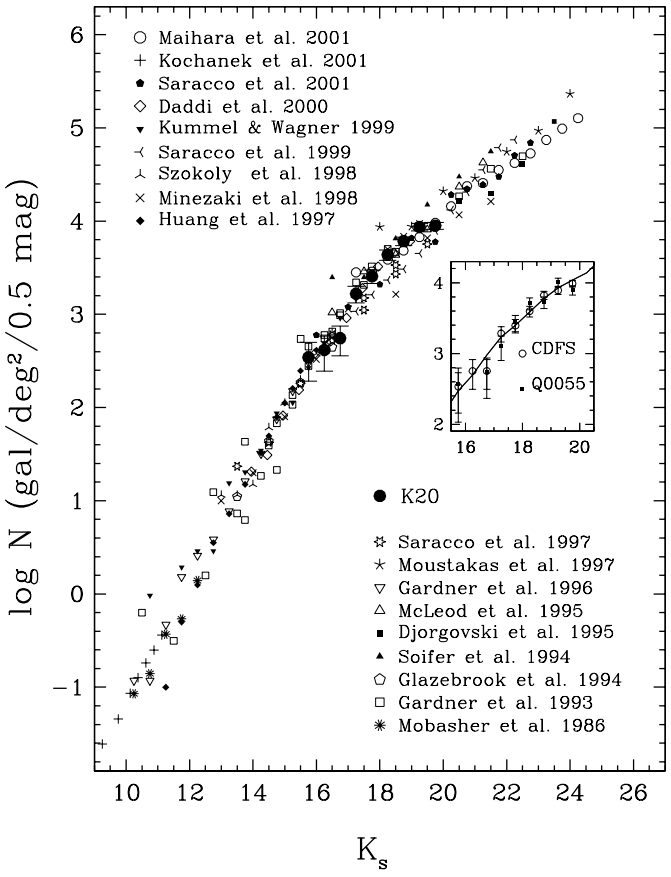

Fig. 5. Differential K_s-band galaxy counts. The filled circles represent the K20 survey counts. Literature survey counts are shown with different symbols. The insert plot shows the counts separately for the CDFS and the 0055-269 field, and the continuous line represents the average K_s-band galaxy counts taken from Hall et al. (1998).

catalog has then been obtained on these "dimmed" images with the same parameters used for the original one. This method tests the whole photometric procedure using a set of objects with clustering and with a wide variety of morphological properties representative of the real galaxy population.

These simulations have shown that: *a)* the flux fraction lost by the BEST magnitudes is negligible to about $K_s = 19.5$, whereas a slight underestimate of 0.05–0.1 magnitudes is present in the fainter side of the sample $19.5 < K_s < 20.0$; *b)* 100% of the objects at $K_s = 20$ are robustly detected in both fields, irrespective of their morphology, although *c)* the scatter between the input and the recovered magnitudes is typically 0.1 magnitudes at $K_s > 19.5$. As a result, *d)* the number counts observed in both fields are not affected by significant instrumental incompleteness.

4.3. Galaxy counts and colors

Table 2 lists the galaxy differential counts in 0.5 magnitude bins in our survey, and Fig. 5 shows a comparison with a compilation of literature counts. No corrections for incompleteness were applied to our data, and we excluded the AGNs and the stars with spectroscopic identification in our sample. The 1σ Poissonian uncertainties of the counts were estimated according to the prescriptions of Gehrels (1986). Our counts are in very good agreement with those of previous surveys.

On the basis of what discussed in previous Sections, the slight flattening shown by our data for $K_s > 19.5$ should not be due to incompleteness, but is likely to be due to field-to-field fluctuations which, as Fig. 5 shows, are the dominant source of scattering in the counts from survey to survey. This is supported by the fact that the small drop in our total counts to $K_s > 19.5$ is seen in only one of our two fields (the 0055-269 field) (see Fig. 5).

The detailed color properties of the galaxies in the K20 sample will be discussed elsewhere. Here, as an additional check of the photometry, we show a comparison between the $R-K_s$ galaxy colors of the galaxies in the K20 sample (the same color used to select the K20 ERO sample discussed in Cimatti et al. 2002 and Daddi et al. 2002) and the sample taken from the Caltech Faint Galaxy Redshift Survey (CFGRS; Cohen et al. 1999a, 1999b), a spectroscopic survey of a complete sample of $K_s < 20.0$ galaxies over a field of 14.6 arcmin^2.

Figure 6 shows a comparison between the $R - K_s$ color distributions. As suggested by Fig. 6 (top panel), such a comparison may be biased by the presence of three clusters (or rich groups) of galaxies present in both surveys: one at $z = 0.67$ and one at $z = 0.73$ in the 0055-269 and in the CDFS respectively, and one at $z = 0.58$ in the CFGRS. To investigate this possibility, we excluded the members of the richest clusters in both samples (Fig. 6 bottom panel). As Fig. 6 (bottom panel) clearly suggests, a Kolmogorov-Smirnov test indicates that the hypothesis that the two distributions are drawn from the same population cannot be rejected at a confidence level of 0.05, thus demonstrating that the difference (Fig. 6, top panel) was due to color biases introduced by the galaxy clusters (or groups).

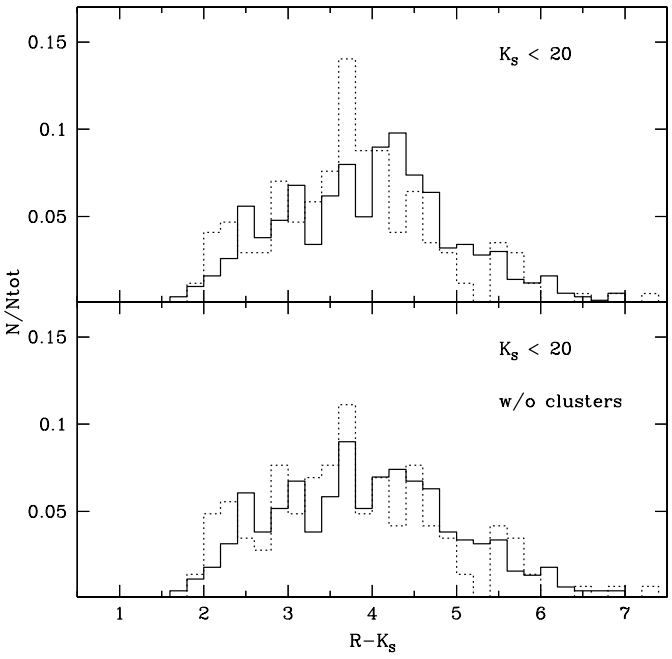

Fig. 6. Top panel: the K20 and the CFGRS (Cohen et al. 1999a, 1999b) survey $R - K_s$ color distributions for $K_s < 20.0$ galaxies (continuous and dotted lines respectively). Bottom panel: the comparison between the K20 and the CFGRS $R - K_s$ color distributions after removing the richest clusters in the two samples.

5. Optical spectroscopy

Optical multi-object spectroscopy was obtained with the ESO VLT UT1 and UT2 equipped respectively with FORS1 (with MOS mode: 19 movable slitlets) and FORS2 (with MXU mode: up to 52 targets observed through a laser-cut slit mask) during 0.5″–2.0″ seeing conditions and with 0.7″–1.2″ wide slits depending on the seeing. The grisms 150I, 200I, 300I were used, providing dispersions of 5.5, 3.9, 2.6 Å/pixel and spectral resolutions of $R = 260$, 380, 660 respectively. The integration times ranged from 0.5 to 3 hours. Dithering of the targets along the slits between two fixed positions was applied as much as possible for the faint target observations in order to efficiently remove the CCD fringing and the strong OH sky lines at $\lambda_{obs} > 7000$ Å.

The data reduction was carried out using IRAF packages. The bias subtraction, overscan correction and flat-fielding were performed in the standard mode. For the non-dithered spectra, the sky background was removed from the two-dimensional frames obtained by fitting a third-order polynomial along the spatial direction and avoiding the regions with object spectra. The resulting sky-subtracted images were kept for following analysis in the course of the redshift determination. The 1D spectra were then optimally extracted and wavelength calibrated using exposures of He-Hg-Ar lamps, taken with the same instrumental configuration. Finally, the spectra were flux-calibrated using standard spectrophotometric stars, de-reddened for atmospheric extinction, corrected for telluric absorptions and scaled to the total R-band magnitudes.

The spectroscopic analysis of the optical spectra and the redshift estimates were done using IRAF tasks, both automatic (`xcsao`) and interactive ones (`rvidlines` and `splot`), and always through visual inspection of the 1D and 2D spectra.

We followed different approaches in the redshift measurements, according to the quality and type of the analyzed spectrum. In case of a spectrum with emission lines, the redshift was obtained with `rvidlines` by means of multiple Gaussian fitting of the spectral features. For the objects with fairly good signal–to–noise ratio and with an absorption line dominated spectrum, we performed an automatic cross-correlation with `xcsao`. As templates for the cross-correlation we used the set of Kinney et al. (1996) template spectra and also high S/N composite spectra obtained from our own K20 survey database. For objects with both emission and absorption lines, we used both `rvidlines` and `xcsao`. For spectra with poor S/N ratio, with a single emission line and/or uncertain spectral features, the redshift was estimated both by checking the reality of the structures on the 2D frames and interactively measuring the wavelengths of the features using `splot` and cross-checking the results with `rvidlines`. Several and independent cross-checks on ambiguous cases were done independently by 2-3 of us in order to ensure independent redshift estimates and to eliminate discrepant cases. Objects with multiple observations made in different mask configurations or different runs provided always consistent results in terms of detected features and redshift measurements, and their spectra were then coadded to increase the final signal-to-noise ratio.

The spectroscopic redshifts were divided into two categories: "high-quality and secure" redshifts (when several features were detected at high significance), and "lower-quality" redshifts (when only one weak emission line was detected and ascribed to [OII]λ3727 emission, or when the detected spectral features were more marginal). Objects with "lower-quality" redshifts are 5% of the total sample to $K_s \leq 20.0$, whereas their fractions decrease to 4% and 2% for $K_s \leq 19.5$ and $K_s \leq 19.0$ respectively. One of the following spectral classes was preliminarly assigned to each object: star, type 1 (i.e. with broad lines) AGN, emission line galaxy, early-type galaxy with emission lines, early-type galaxy with no emission lines. Figure 7 shows examples of the different spectral types. A more detailed spectral classification is under way and will be presented together with the K20 spectroscopic catalog.

6. Near-infrared spectroscopy

A small fraction (22 objects, 3.9%) of the K20 sample was observed with near-IR spectroscopy using the VLT UT1+ISAAC (Moorwood et al. 1999) in order to derive the redshifts of the galaxies which were too faint for optical spectroscopy and/or expected to be in a redshift range difficult for optical spectroscopy.

During the first ISAAC run (Table 3), targets in the CDFS were selected according to the photometric redshifts available at that time in order to search mostly for Hα emission redshifted in the H-band for $1.3 < z < 1.8$. The observations were carried out under photometric and 0.5″–1.5″ seeing conditions. The low spectral resolution mode ($R = 500$ with 1″ slit) was adopted in order to maximize the covered spectral range per integration, the slit was 1″ wide, providing a spectral

Table 3. The VLT spectroscopic runs.

Dates	Telescope	Instrument	Mode	Multiplex	Seeing range	Run completion
1999 01-05.10	UT1	FORS1	MOS	≤19	1.0″–2.5″	50%
1999 06-09.11	UT1	FORS1	MOS	≤19	0.4″–1.5″	100%
1999 28-30.11	UT1	ISAAC	LR	≤2	0.5″–1.5″	100%
2000 24-28.11	UT2	FORS2	MXU	≤52	0.4″–1.5″	100%
2000 04-08.12	UT1	ISAAC	LR	≤2	0.5″–2.0″	50%

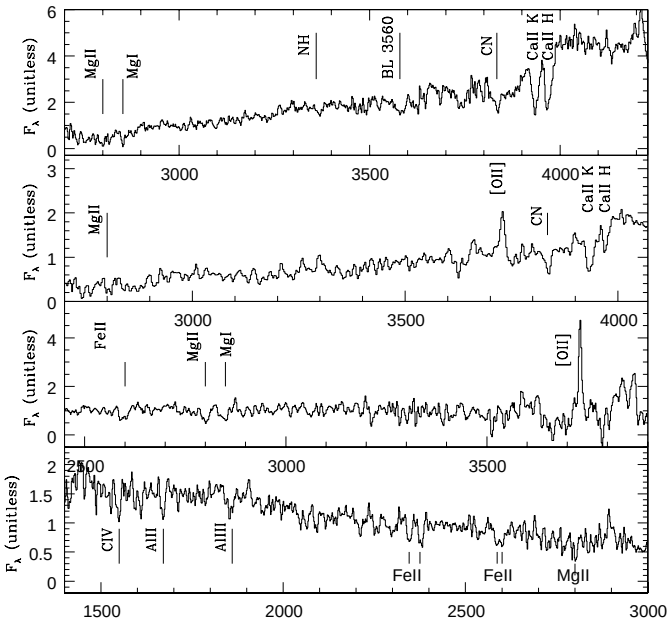

Fig. 7. Examples of high-z galaxies with the four adopted spectral classifications. From top to bottom: an early-type at $z = 1.096$ ($R = 23.0$), an early-type + [OII]λ3727 emission at $z = 0.735$ ($R = 23$), an emission line galaxy at $z = 1.367$ ($R = 23.0$), an absorption line galaxy at $z = 1.725$ ($R = 23.5$). Some typical absorption and emission lines are also indicated for each spectrum.

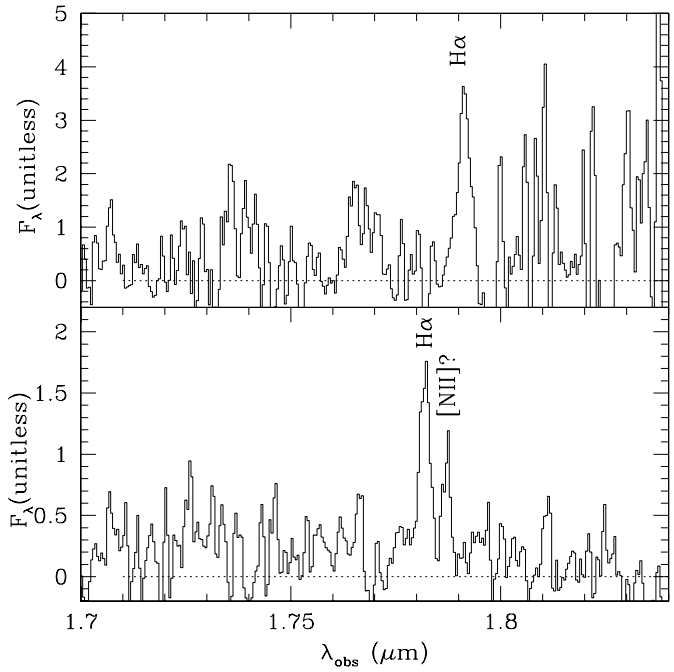

Fig. 8. ISAAC H-band low resolution spectra of two emission line galaxies with Hα redshifted at $z = 1.729$ (top panel) and $z = 1.715$ (bottom panel).

resolution *FWHM* of 32 Å in H-band. The observations were done by nodding the target(s) along the slit between two positions A and B with a typical nod throw of 10–20″. The integration time was 10 min per position. For instance, a total integration time of 1 hour was obtained following a pattern ABBAAB. Whenever possible, two targets were observed simultaneously in the slit in order to maximize the multiplex. The spectral frames were flat-fielded, rectified, sky-subtracted, coadded and divided by the response curve obtained using the spectra of O stars. Absolute flux calibration was achieved by normalizing the spectra to the JK_s broad-band photometry or to the interpolated H-band magnitude in case of H-band spectra.

During the second ISAAC run (Table 3), the targets were selected from the CDFS and the 0055-269 fields whenever their spectra did not show features in the optical and if the photometric redshifts suggested $z > 1.3$. The observations were carried out as for the first run. Despite a large fraction of the time lost because of bad weather and poor seeing, such a run was more successful in identifying a few high-z star-forming galaxies thanks to their Hα emission.

The bottom line for the ISAAC runs is that the absence of a multi-object spectroscopic mode, being each integration limited to a single band (J or H or K), and the lack of very accurate photometric redshifts at the time of the observations made it difficult to derive a substantial number of spectroscopic redshifts based on near-IR spectroscopy alone. All in all, redshifts were derived for four galaxies at $1.3 < z < 1.9$ out of the 22 observed (see Fig. 8 for two examples of successful ISAAC observations).

7. Spectroscopic completeness

Table 4 summarizes the status of the sample and of the spectroscopic redshift identifications.

Only about 6% of the sample targets to $K_s = 20$ were not observed either because it was not possible to fit them in the observing masks or because too faint in the optical bands or because of the nights lost due to bad weather or bad seeing conditions.

The efficiencies in deriving the spectroscopic redshifts ($N_{\rm identified}/N_{\rm observed}$) was 96%, 91% and 85% for $K_s \leq 19.0$, $19.0 < K_s \leq 19.5$ and $19.5 < K_s \leq 20.0$ respectively,

Table 4. Summary of the spectroscopic results.

Magnitude	Field	$N_{\rm total}$	$N_{\rm observed}$	$N_{\rm identified}$	$\frac{N_{\rm identified}}{N_{\rm total}}$	$\frac{N_{\rm identified}}{N_{\rm observed}}$	$N_{\rm galaxies}$	$N_{\rm AGN}$	$N_{\rm stars}$
$K_{\rm s} \leq 19.0$	0055-269	97	95	92	0.95	0.97	81	4	7
	CDFS	180	176	168	0.93	0.95	137	5	26
	TOTAL	277	271	260	0.94	0.96	218	9	33
$19.0 < K_{\rm s} \leq 19.5$	0055-269	58	56	49	0.84	0.88	47	0	2
	CDFS	75	73	69	0.92	0.95	63	2	4
	TOTAL	133	129	118	0.85	0.91	118	2	6
$19.5 < K_{\rm s} \leq 20.0$	0055-269	43	31	26	0.60	0.84	26	0	0
	CDFS	93	82	70	0.75	0.85	63	1	6
	TOTAL	136	113	96	0.71	0.85	89	1	6
$K_{\rm s} \leq 20.0$	0055-269	198	182	167	0.84	0.92	154	4	9
	CDFS	348	331	307	0.88	0.93	263	8	36
	TOTAL	546	513	474	0.87	0.92	417	12	45

whereas the overall spectroscopic redshift completeness ($N_{\rm identified}/N_{\rm total}$) in the same magnitude ranges is 94%, 85% and 71%.

The spectroscopic completeness of the total $K_{\rm s} \leq 20.0$ sample is 87% and is one of the highest reached for samples of faint K-selected galaxies.

8. Optical imaging and photometric redshifts

The availability of high-quality and deep imaging (besides the $K_{\rm s}$ images) and of spectroscopic redshifts covering also the critical region of $1.3 < z < 1.9$ allowed us to optimize the estimate of the photometric redshifts in a self-consistent way, and to obtain the most reliable information possible on the redshifts of the targets with no spectroscopic z or with no observations available.

Although the final multicolor data set is not homogeneous (in terms of bandwidths and depth) over the two fields, the strategy followed in both fields is identical, aimed at assuring that the UV and optical coverage and depth are adequate to follow the spectral shape of the reddest galaxies in the sample. In practice, we have imaged the 0055-269 field over 10 bands ($UBGVRR_{\rm w}IzJK_{\rm s}$), obtained with the ESO NTT + SUSI2 ($UBGVR_{\rm w}I$) and SOFI (J), and VLT + FORS1 (R and z), for a total of about 45 hours of integration. In the CDFS field, we used a combination of public EIS NTT data (U) and deep FORS1 images ($BVRIz$) obtained in the framework of a different program (courtesy of P. Rosati & M. Nonino). Unfortunately, the FORS1 images do not overlap completely with the area surveyed here, so that multicolor imaging and photometric redshifts are available for a subset of 272 over 348 objects in the CDFS. In addition, and at variance with the 0055-269 field, the multicolor catalog of the CDFS is not in its final form, since we plan to eventually include the forthcoming J EIS public images, but the current ($UBVRIzK$) data set already provides a highly satisfactory solution for photometric redshifts.

For the purpose of estimating photometric redshifts and deriving the Spectral Energy Distributions (SEDs) of the target galaxies, we developed a technique to obtain a seeing–corrected "optimal" aperture photometry to cope with the inhomogeneous image quality over the different bands. Photometric redshifts have been obtained through template fitting (see Fontana et al. 2000 et al. for the details), using in this case the PEGASE 2.0 template spectral package (Fioc & Rocca–Volmerange 1999).

The whole procedure has been tested against the sample with secure spectroscopic redshift, and the results are shown in Figs. 9–10 The comparison between spectroscopic and photometric redshifts shows that it is possible to achieve a high reliability and accuracy even with ground–based data sets, provided that the imaging data are of adequate quality.

The results in the two fields are slightly different, because of the different quality of the imaging data set. To compute a suitable statistics on $z_{\rm spe} - z_{\rm phot}$, one has to define a recipe to account for the non-Gaussian shape of its distribution function. The one we adopt here is to compute mean values and standard deviations of $z_{\rm spe} - z_{\rm phot}$ on all the objects with a fractional error $\Delta z = (z_{\rm spe} - z_{\rm phot})/(1 + z_{\rm spe})$ smaller (in modulus) than 0.15. This choice is based on the fact that the fractional error Δz is roughly constant with redshift with a σ–clipped dispersion of about 0.05 in both these samples and in the HDFN (Cohen et al. 2000; Fontana et al. 2002). The corresponding selection is delimited by the two dashed lines in Fig. 9. Objects outside this range can be described as "outliers". As it emerges from Fig. 9, most of the objects lie within the boundaries that we use to define the "satisfactory" fits, and most of the outliers are close to the same boundaries.

In the 0055-269 field, the number of outliers is fairly small (7 over 140), and the rms dispersion of the remaining fraction in the range $0 < z < 2$ is $\sigma_{\Delta z} = 0.078$, with a median value $< \Delta z > = -0.004$, very close to the values obtained in the HDF–N over the same redshift range and with the same template set (Fontana et al. 2000). In the case of the CDFS, we reached a final accuracy of $\sigma_{\Delta z} = 0.095$ with a median value $< \Delta z > = 0.02$, with a fraction of discrepant objects of 13 over the 198 galaxies with secure redshifts used in the comparison.

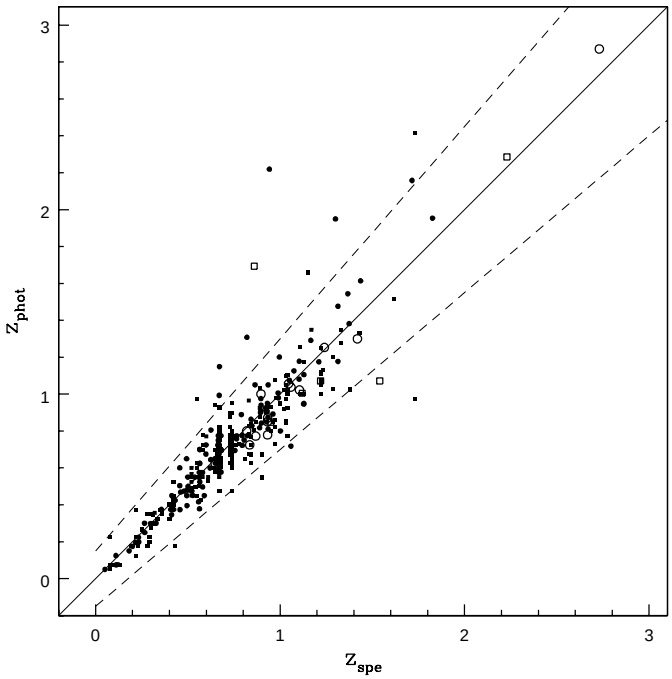

Fig. 9. The comparison between spectroscopic (x–axis) and photometric (y–axis) redshifts of the galaxies in the K20 survey: 140 galaxies with secure redshifts in the 0055-269 field indicated by filled circles and 198 galaxies in the CDFS indicated by filled squares. The solid line shows the $z_{\rm spe} = z_{\rm phot}$ relation. The two dashed line delimit the region where $|z_{\rm spe} - z_{\rm phot}| \leq 0.15(1 + z_{\rm spe})$, that has been used to compute the overall statistics in the sample (see text for details). The open symbols indicate objects with "lower quality" spectroscopic redshifts.

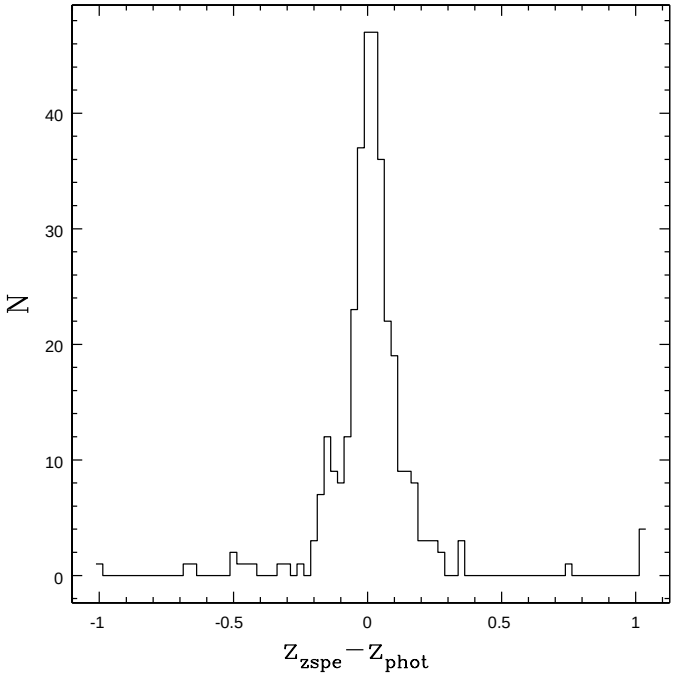

Fig. 10. The histogram of the observed scatter $z_{\rm spe} - z_{\rm phot}$ for all the galaxies of the sample with spectroscopic redshift.

It is also important to notice that objects with "lower quality" spectroscopic redshifts (see Sect. 5) generally follow the relation between photometric and spectroscopic redshifts (Fig. 9).

In both cases, the high accuracy and the low level of misidentified objects allow us to use the photometric redshift estimate both to support the redshift identification of objects with uncertain spectroscopic redshift, and to adopt the photometric redshift for the unobserved/unidentified objects.

The dispersion on the global sample (CDFS + 0055-269 fields) is $\sigma = 0.089$ and the average is $< z_{\rm spe} - z_{\rm phot} > = 0.012$.

In the whole K20 database, there are only 9 objects (in the CDFS) for which neither $z_{\rm spe}$ nor $z_{\rm phot}$ are available. Thus, the overall redshift completeness reached for our sample by using both $z_{\rm spe}$ and $z_{\rm phot}$ is 537/546 = 98.3%.

9. Release of the $K_{\rm s}$-band photometric catalog

We make the $K_{\rm s}$-band photometric sample available at the web site `http://www.arcetri.astro.it/~k20/releases/`. This version of the sample includes for the moment only the names of the targets, the coordinates, the total (BEST) $K_{\rm s}$-band magnitudes and their photometric uncertainties. An extract of such catalog is shown in Table 5. In the next papers, we will also release the full spectroscopic and multicolor catalogs.

10. Summary

We discussed the general scientific background and aims of the K20 survey and we described the sample photometric and spectroscopic properties.

The relevant advantages of the K20 database are the small K-correction effects due to the $K_{\rm s}$-band selection, its size (about 500 galaxies), the distribution of the targets in two independent fields, the use of near-IR spectroscopy for a subsample of the targets, and the availability of a large deep imaging database from the optical to the near-IR.

Extensive simulations show that the sample is highly complete to $K_{\rm s} = 20.0$ and not affected by strong selection effects on the galaxy population, with the possible exception of a slight underestimate of the total flux for large and luminous early-type galaxies with de Vaucouleurs surface brightness profiles. Such a selection effect can be taken into account when comparing the observed K20 sample with model predictions. The observed galaxy counts and the $R - K_{\rm s}$ color distribution are in agreement with literature results.

Optical spectroscopy, aided by near-IR spectroscopy, allowed us to achieve a high redshift completeness for a sample of galaxies selected in the near-IR (94% to $K_{\rm s} < 19.0$ and 87% $K_{\rm s} < 20.0$), and to obtain spectroscopic redshifts in the "desert" of $1.4 < z < 2.2$.

The high-quality deep imaging database allowed us also to obtain tested and reliable photometric redshifts for the unobserved or spectroscopically unidentified galaxies. Using the photometric redshifts, the global completeness ($z_{\rm spe} + z_{\rm phot}$) increases to 98.3% of the total sample.

Table 5. Extract of the K_s-band photometric catalog of the 0055-269 field.

ID	Right Ascension (J2000)	Declination (J2000)	K_s	$\sigma(K_s)$
00013	00:57:55.27	−26:40:58.3	18.83	0.03
00017	00:57:58.24	−26:40:59.6	19.68	0.07
00018	00:58:02.90	−26:41:01.5	16.16	0.01
00019	00:58:06.68	−26:40:59.7	18.98	0.04
00021	00:57:51.54	−26:41:03.6	18.54	0.03
00022	00:57:59.53	−26:41:04.6	19.19	0.05
00023	00:57:56.82	−26:41:05.2	19.87	0.08
00024	00:57:54.74	−26:41:07.9	19.94	0.06
00025	00:57:54.52	−26:41:09.7	18.46	0.02
.....	.....	.....	.....	....

Such a rich photometric and spectroscopic database makes the K20 sample a key tool to investigate the formation and evolution of galaxies.

Acknowledgements. We thank the VLT support astronomers for their kind assistance and competent support during the observations. AC warmly thanks ESO (Garching) for the hospitality during his visits. We thank J. Cohen for providing the CFGRS sample in digital form. We warmly thank Piero Rosati and Mario Nonino for providing the reduced and calibrated *BVRI* FORS1 images of the CDFS. We also thank the anonymous referee for the useful comments. The imaging observations of the 0055-269 field were performed during SUSI2 guaranteed time of the Observatory of Rome in the framework of the ESO-Rome Observatory agreement for this instrument.

References

Angeretti, L., Pozzetti, L., & Zamorani, G. 2002, in A new era in cosmology, Durham, UK, ASP Conf. Ser., ed. N. Metcalfe, & T. Shanks, in press
Baugh, C. M., Cole, S., & Frenk, C. S. 1996, MNRAS, 283, 1361
Baugh, C. M., Benson, A. J., Cole, S., et al. 2002, in The Mass of Galaxies at Low and High Redshift, Venice 2001, ed. R. Bender, & A. Renzini, in press [astro-ph/0203051]
Bender, R., Burstein, D., & Faber, S. M. 1992, ApJ, 399, 462
Bertin, E., & Arnouts, S. 1996, A&A, 117, 393
Broadhurst, T. J., Ellis, R. S., & Glazebrook, K. 1992, Nature, 355, 55
Bruzual, G., & Charlot, S. 1993, 405, 538
Cimatti, A., Daddi, E., Mignoli, M., et al. 2002, A&A, 381, L68
Cohen, J. G., Blandford, R., Hogg, D. W., Pahre, M. A., & Shopbell, P. 1999a, ApJ, 512, 30
Cohen, J. G., Hogg, D. W., Pahre, M. A., et al. 1999b, ApJS, 120, 171
Cohen, J. G., Hogg, D. W., Blandford, R., et al. 2000, ApJ, 538, 29
Cole, S., Lacey, C. G., Baugh, C. M., & Frenk, C. S. 2000, MNRAS, 319, 168
Cole, S., Norberg, P., Baugh, C. M., et al. 2001, MNRAS, 326, 255
Cowie, L. L., Gardner, J. P., Hu, E. M., et al. 1994, ApJ, 434, 114
Cowie, L. L., Songaila, A., Hu, E. M., & Cohen, J. G. 1996, AJ, 112, 839
Daddi, E., Cimatti, A., Pozzetti, L., et al. 2000, A&A, 361, 535
Daddi, E., Broadhurst, T., Zamorani, G., et al. 2001, A&A, 376, 825
Daddi, E., Cimatti, A., Broadhurst, T., et al. 2002, A&A, 384, L1
Dalcanton, J. J. 1998, ApJ, 495, 251
Djorgovski, S., Soifer, B. T., Pahre, M. A., et al. 1995, ApJ, 438, L13
Drory, N., Bender, R., Snigula, J., et al. 2001, ApJ, 562, L111
Fasano, G., Cristiani, S., Arnouts, S., & Filippi, M. 1998, AJ, 115, 1400
Firth, A. E., Somerville, R. S., McMahon, R. G., et al. 2001, MNRAS, submitted [astro-ph/0108182]
Fontana, A., Menci, N., D'Odorico, S., et al. 1999, MNRAS, 310, L27
Fontana, A., et al. 2002, A&A, submitted
Fontana, A., D'Odorico, S., Poli, F., et al. 2000, AJ, 120, 2206
Gardner, J. P., Cowie, L. L., & Wainscoat, R. J. 1993, ApJ, 415, L9
Gardner, J. P., Sharples, R. M., Carrasco, B. E., & Frenk, C. S. 1996, MNRAS, 282, L1
Gavazzi, G., Pierini, D., & Boselli, A. 1996, A&A, 312, 397
Gehrels, N. 1986, ApJ, 303, 336
Giacconi, R., Rosati, P., Tozzi, P., et al. 2001, ApJ, 551, 624
Glazebrook, K., Peacock, J. A., Collins, C. A., & Miller, L. 1994, MNRAS, 266, 65
Hall, P. B., Green, R. F., & Cohen, M. 1998, ApJS, 119, 1
Huang, J.-S., Cowie, L. L., Gardner, J. P., et al. 1997, ApJ, 476, 12
Impey, C. D., Sprayberry, D., Irwin, M. J., & Bothun, G. D. 1996, ApJS, 105, 209
Impey, C. D., & Bothun, G. D. 1997, ARA&A, 35, 267
Kauffmann, G., White, S. D. M., & Guiderdoni, B. 1993, MNRAS, 264, 201
Kauffmann, G. 1996, MNRAS, 281, 487
Kauffmann, G., & Charlot, S. 1998, MNRAS, 297, L23
Kinney, A. L., Calzetti, D., Bohlin, R. C., et al. 1996, ApJ, 467, 38
Kochanek, C. S., Pahre, M. A., Falco, E. E., et al. 2001, ApJ, 560, 566
Kron, R. G. 1980, ApJS, 43, 305
Kümmel, M. W., & Wagner, S. J. 2000, A&A, 353, 867
Lilly, S. J., Le Fevre, O., Crampton, D., Hammer, F., & Tresse, L. 1995, ApJ, 455, 50
Madau, P., Pozzetti, L., & Dickinson, M. 1998, ApJ, 498, 106
Maihara, T., et al. 2001, PASJ, 53, 25
Marleau, F. R., & Simard, L. 1998, ApJ, 507, 585
Martini, P. 2001, AJ, 121, 598
McLeod, B. A., Bernstein, G. M., Rieke, M. J., Tollestrup, E. V., & Fazio, G. G. 1995, ApJS, 96, 117
Minezaki, T., Kobayashi, Y., Yoshii, Y., & Peterson, B. A. 1998, ApJ, 494, 111
Mobasher, B., Ellis, R. S., & Sharples, R. M. 1986, MNRAS, 223, 11

Moorwood, A. F. M., Cuby, J.-G., & Lidman, C. 1998, The Messenger, 91, 9
Moorwood, A. F. M., et al. 1999, The Messenger, 95, 1
Moustakas, L. A., Davis, M., Graham, J. R., et al. 1997, 475, 445
Pahre, M. A. 1999, ApJS, 124, 127
Peebles, P. J. E. 2002, in A new era in cosmology, Durham, U.K., ASP Conf. Ser., ed. N. Metcalfe, & T. Shanks, in press [astro-ph/0201015]
Persson, S. E., Murphy, D. C., Krzeminski, W., Roth, M., & Rieke, M. J. 1998, AJ, 116, 2475
Rengelink, R., et al. 1998, A&A, submitted [astro-ph/9812190]
Renzini, A. 1999, in The formation of galactic bulges, ed. C. M. Carollo, H. C. Ferguson, & R. F. G. Wyse (Cambridge, U.K., Cambridge University Press), 9
Renzini, A., & Cimatti, A. 1999, in The Hy-Redshift Universe: Galaxy Formation and Evolution at High Redshift, Berkeley, USA, ASP Conf. Proc. 193, ed. A. J. Bunker, & W. J. M. van Breugel, 312
Rudnick, G., Franx, M., Rix, H.-W., et al. 2001, AJ, 122, 2205
Saracco, P., Iovino, A., Garilli, B., Maccagni, D., & Chincarini, G. 1997, AJ, 114, 887
Saracco, P., D'Odorico, S., Moorwood, A., et al. 1999, A&A, 349, 751
Saracco, P., Giallongo, E., Cristiani, S., et al. 2001, A&A, 375, 1
Scalo, J. M. 1986, Fund. Cosm. Phys., 11, 1
Schlegel, D. J., Finkbeiner, D. P., & Davis, M. 1998, ApJ, 500, 525
Soifer, B. T., et al. 1994, ApJ, 420, L1
Somerville, R. S., Primack, J. R., & Faber, S. M. 2001, MNRAS, 320, 504
Songaila, A., Cowie, L. L., Hu, E. M., & Gardner, J. P. 1994, ApJS, 94, 461
Stern, D., Connolly, A., Eisenhardt, P., et al. 2001, in Deep Fields, Proceedings of the ESO Workshop (Garching, Germany, Springer-Verlag), 76
Szokoly, G. P., Subbarao, M. U., Connolly, A. J., & Mobasher, B. 1998, ApJ, 492, 452
van Dokkum, P. G., & Stanford, S. A. 2001, ApJ, 562, L35